Hindawi
Adsorption Science & Technology
Volume 2022, Article ID 6999213, 9 pages
https://doi.org/10.1155/2022/6999213

Research Article

Adsorption Mechanism and Electrochemical Characteristic of Methyl Blue onto Calcium Ferrite Nanosheets

Shaoshuai Zhang,[1] **Shuping Xu**,[2] **Yun Ni**,[1] **Ziye Zhu**,[1] **Chen Ling**,[1] **and Ruijiang Liu**[1]

[1]*School of Pharmacy, Jiangsu University, Zhenjiang 212013, China*
[2]*The People's Hospital of Danyang, Affiliated Danyang Hospital of Nantong University, Zhenjiang 212300, China*

Correspondence should be addressed to Ruijiang Liu; luckystar_lrj@ujs.edu.cn

Received 26 July 2022; Accepted 30 August 2022; Published 16 September 2022

Academic Editor: Muhammad Raziq Rahimi Kooh

A rapid combustion process was applied to prepare $CaFe_2O_4$ nanomaterials using $CaBr_2{\cdot}xH_2O$ and $Fe(NO_3)_3{\cdot}9H_2O$ as raw materials and $CaFe_2O_4$ nanomaterials were characterized by SEM, TEM, VSM, XRD, and FTIR techniques. The results showed that the prepared nanomaterials had a sheet-like structure, and for larger adsorption capacity of dyes, $CaFe_2O_4$ nanosheets prepared at 700°C for 2 h with average grain size was 93.3 nm, a thickness of 8.4 nm, and the saturation magnetization of 8.15 emu/g were employed as adsorbate for the removal of methyl blue (MB). The adsorption performance of MB onto $CaFe_2O_4$ nanosheets was investigated; $CaFe_2O_4$ nanosheets displayed favorable adsorption capacity, and the adsorption conformed to the pseudo-second-order model and the Freundlich model, which demonstrated that the adsorption process of MB on $CaFe_2O_4$ nanosheets belonged to multilayer chemisorption process. When the pH value reached 3, the adsorption capacity of MB by $CaFe_2O_4$ nanosheets kept maximum value of 478.07 mg/g; and after 5 regenerations, the removal efficiency of MB was reduced to 59.06% of the first time. The electrochemical behavior of MB onto the nanosheets was evaluated through CV in conjunction with EIS. The $CaFe_2O_4$ nanosheets revealed a promising prospect for the adsorption of dyes.

1. Introduction

Magnetic materials have widespread applications, such as electronics, automotive, environmental protection, and new energy sources [1–8]. Magnetic materials are divided into categories by nature: metallic and nonmetallic, the former mainly having metallic magnets such as $Nd_2Fe_{14}B$ and nickel-based alloys [9–12], the latter mainly being ferrite nanomaterials [13, 14]. Compared to metallic materials, ferrite, as a nonmetallic material, is cheap, technical maturity and stable performance, and is, therefore, used in a significant amount. In the realm of magnetic nanomaterials, ferrite nanomaterials are composite oxide consisting of iron in combination with one or more other suitable metallic elements. The most applied ferrite is the spinel type with the chemical formula MFe_2O_4 or $MO{\cdot}Fe_2O_3$ (M = Mg, Mn, Co, Zn, Cu, Ca, etc.). M is composed of a divalent mental ion or a plurality of mental ions whose average valence is divalent [15, 16]. Among them, $CaFe_2O_4$ have received extensive attention because Ca^{2+} is not a heavy metal [17].

$CaFe_2O_4$ is *p*-type semiconductor material, which has the advantages of nontoxicity, environmental friendliness, and good biocompatibility [18–20]. At present, there are many methods for preparing $CaFe_2O_4$ nanomaterials, such as solid-phase reaction [21], coprecipitation [22], one-step hydrothermal [23], sol-gel [24], and electrospun [25]. The above methods, however, prepare ferrite products with poor homogeneity, high costs, and complex reactions. Rapid combustion process is a convenient and effective way to prepare polymetallic and monometallic oxides [26]. Compared with the other methods, it has the advantages of cheaper cost, simple manipulation, and controllable particle size.

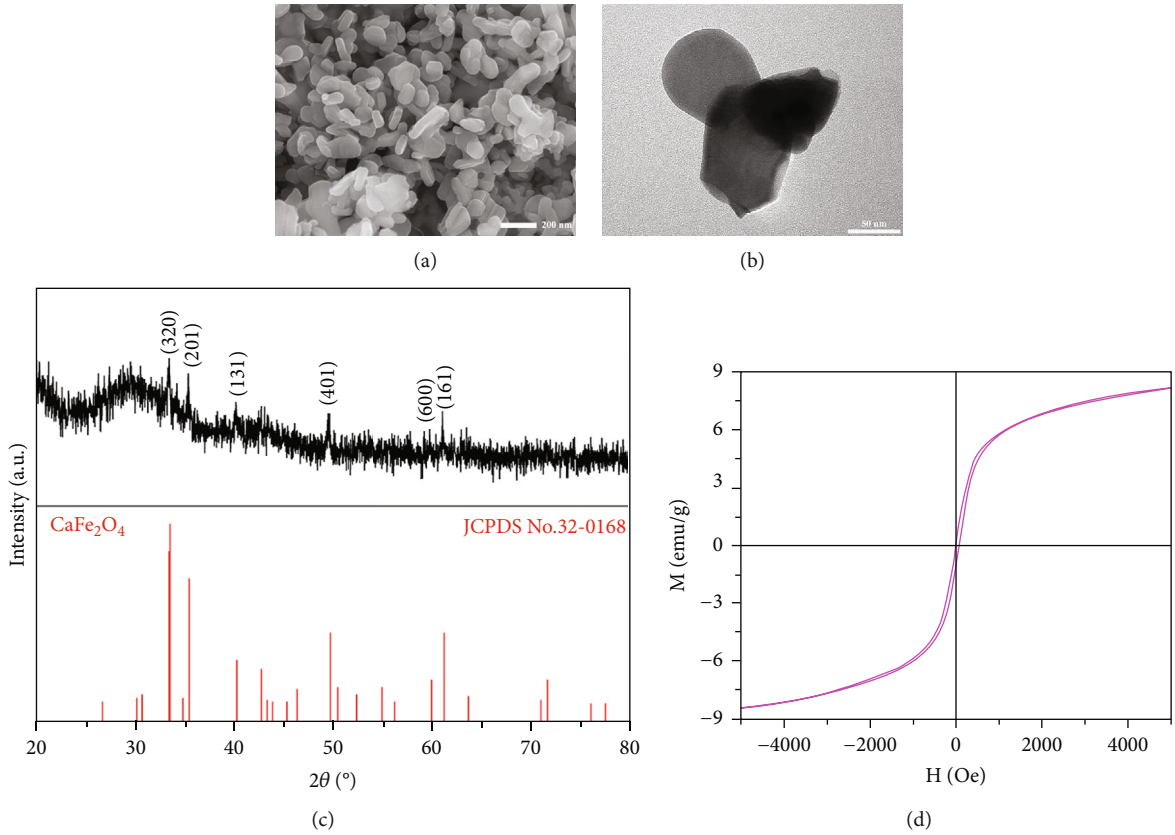

Figure 1: SEM morphology (a) and TEM image (b), XRD pattern (c), and VSM analysis (d) of $CaFe_2O_4$ nanosheets.

Today, there is an increasing demand for dyes and the discharge of dye wastewater is gaining widespread attention. Dye wastewater contains harmful chemicals and is highly toxic, posing a serious risk to human health and safety, [27–29] such as methyl blue (MB) can cause skin irritation, profuse sweating, and cancer, [30]. The removal of dyes from wastewater is therefore urgent. The current methods of treating dyes are adsorption [31], photodegradation [32], and advanced oxidation [33]. Of these, adsorption method is the simplest and most effective technique due to its simplicity of operation, the variety of adsorbents, and environmental friendliness [34–36]. Ferrite nanomaterials have received a lot of attention from researchers as emerging adsorption materials. With a large specific surface area and many active sites, ferrite can quickly achieve solid-liquid separation under the action of an applied magnetic field, effectively avoiding secondary contamination [37].

In this work, an environmentally friendly adsorbent was obtained experimentally with the concept of regeneration and environmentally friendly utilization. $CaFe_2O_4$ nanomaterials were prepared by a rapid combustion approach and characterized, and the adsorption mechanism of MB removal from simulated dye wastewater onto $CaFe_2O_4$ nanosheets was investigated. The prepared $CaFe_2O_4$ nanomaterials could efficiently remove MB from the solutions, which provided a reference for the application of ferrite nanomaterials in the treatment of dye wastewater, and had certain research significance.

2. Materials and Methods

2.1. Preparation and Characterization of $CaFe_2O_4$ Nanomaterials. Analytical grade calcium bromide hydrate ($CaBr_2{\cdot}xH_2O$, 96%) and ferric nitrate nonahydrate ($Fe(NO_3)_3{\cdot}9H_2O$, AR) along with ethyl alcohol (C_2H_6O, AR) were used as raw materials without further purification. Under magnetic agitation, 1.93 g $CaBr_2{\cdot}xH_2O$, 7.66 g $Fe(NO_3)_3{\cdot}9H_2O$, and 50 mL absolute ethanol were blended. Then the mixed solution was burned and put into the programmed temperature-control furnace after the fire was extinguished. The calcination was carried out at 400-800°C, respectively. Finally, the nanomaterials after calcination were ground to get the powders.

Analyzing the characteristic of nanomaterial morphology by scanning and transmission electron microscopy (SEM, JSM-7001F, JEOL Ltd., Japan; TEM, JEM-2100, JEOL Ltd., Japan), X-ray diffraction (XRD, D8 ADVANCE, Germany) was applied to research the physical phase analysis and crystallinity with Cu-Kα and the diffraction angles range from 20-80°. The saturation magnetization was measured by the vibrating sample magnetometer (VSM, HH-15, Physcience Opto-electronics Co., Ltd., Beijing, China). Analysis of the functional groups and chemical bonds of the nanomaterials before and after adsorption by Fourier transform infrared spectra (FTIR, FTIR-370, Nicolet Avatar, America).

2.2. Adsorption Experiment. $CaFe_2O_4$ nanomaterials were added to MB (BS, 99%) solution for adsorption experiments

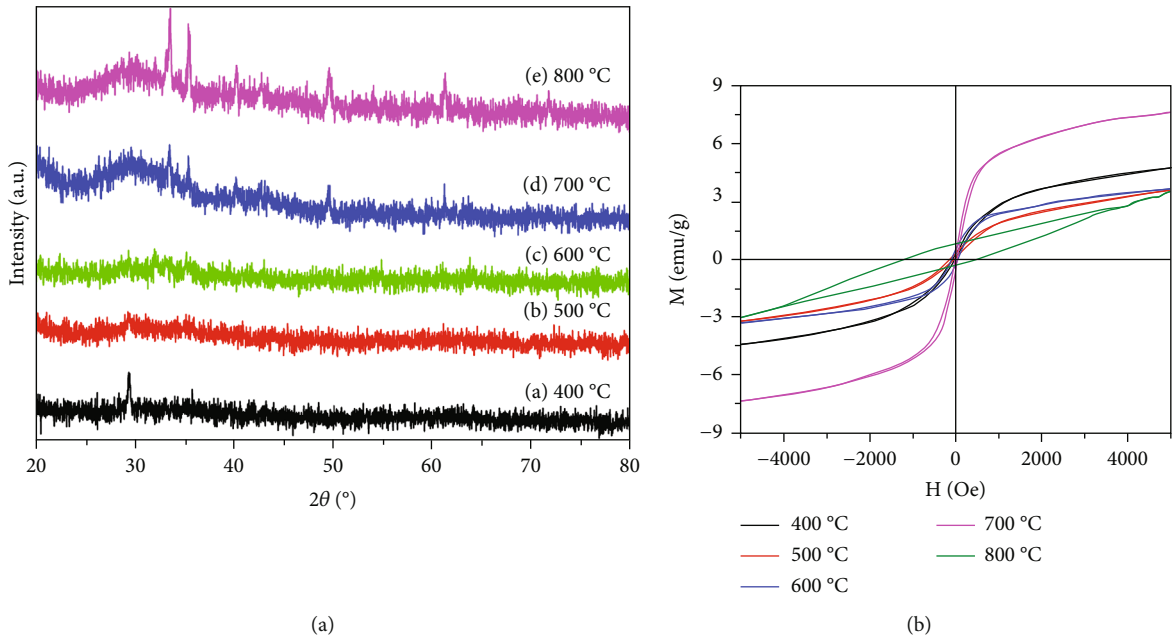

Figure 2: XRD patterns (a) and hysteresis loops (b) of $CaFe_2O_4$ nanomaterials.

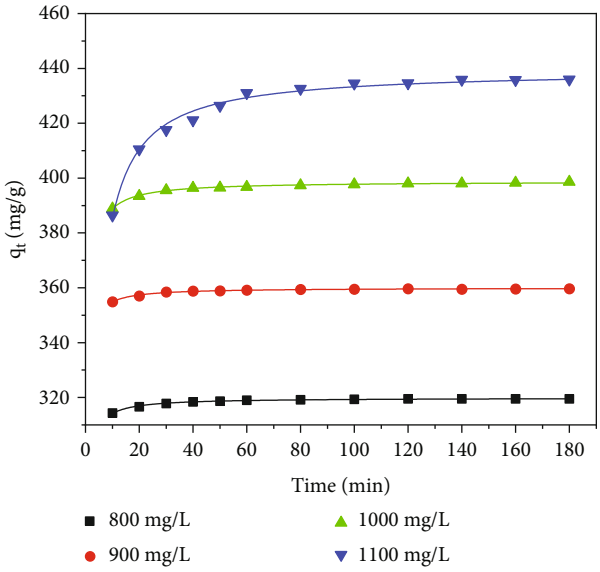

Figure 3: Adsorption kinetics model of $CaFe_2O_4$ nanosheets for MB with different initial concentrations.

to research the effects of different adsorbent times (10-180 min), various pH values (1-9), different initial mass concentrations (800-3000 mg/L), and regeneration times on adsorbent adsorption performance. After the adsorption was completed by centrifugation at 10000 rpm, the supernatant was taken to measure the absorbance using ultraviolet spectrophotometer (UV), and then the remaining concentration was calculated from the MB standard curve, and the corresponding capacity of adsorption was calculated by

$$q = \frac{V(C_0 - C)}{m}, \quad (1)$$

where C_0 and C (mg/L) were the solution concentrations before and after the adsorption of MB, respectively; V (mL) was the MB solution volume; m (g) was the mass of the adsorbent.

2.3. Electrochemical Experiments. An electrochemical workstation was employed to research the electrochemical behavior of $CaFe_2O_4$ nanosheets. Glassy carbon electrode, Ag/AgCl electrode, and platinum wire electrode with good electrical conductivity and chemical stability were employed as experimental electrodes, which play the roles of working, reference, and auxiliary. Cyclic voltammetry (CV) was observed at voltages of −0.2-0.7 V and 100 mV/s scan rate. Electrochemical impedance spectroscopy (EIS) was obtained for signal amplitudes for 5 mV and frequencies in the range 0.1-10000 Hz.

3. Results and Discussion

3.1. Characterizations of Magnetic $CaFe_2O_4$ Nanomaterials. The characteristics of as-prepared $CaFe_2O_4$ nanomaterials were shown in Figure 1. SEM morphology (Figure 1(a)) showed that $CaFe_2O_4$ nanomaterials were irregularly flaky textures. The average grain size of 40.2 nm for $CaFe_2O_4$ nanosheets, but the actual average grain size was 93.3 nm, which indicated that superposition occurred during the preparation process. The average grain size was calculated by the Scherrer formula [13]:

$$D = \frac{0.89\lambda}{\beta \cos\theta}. \quad (2)$$

Where D was the average size of $CaFe_2O_4$ nanosheets (nm); λ was the wavelength of the nanosheets for XRD measurements; β was the half-height width of the diffraction peak of the nanosheets; θ was the Bragg diffraction angle. The

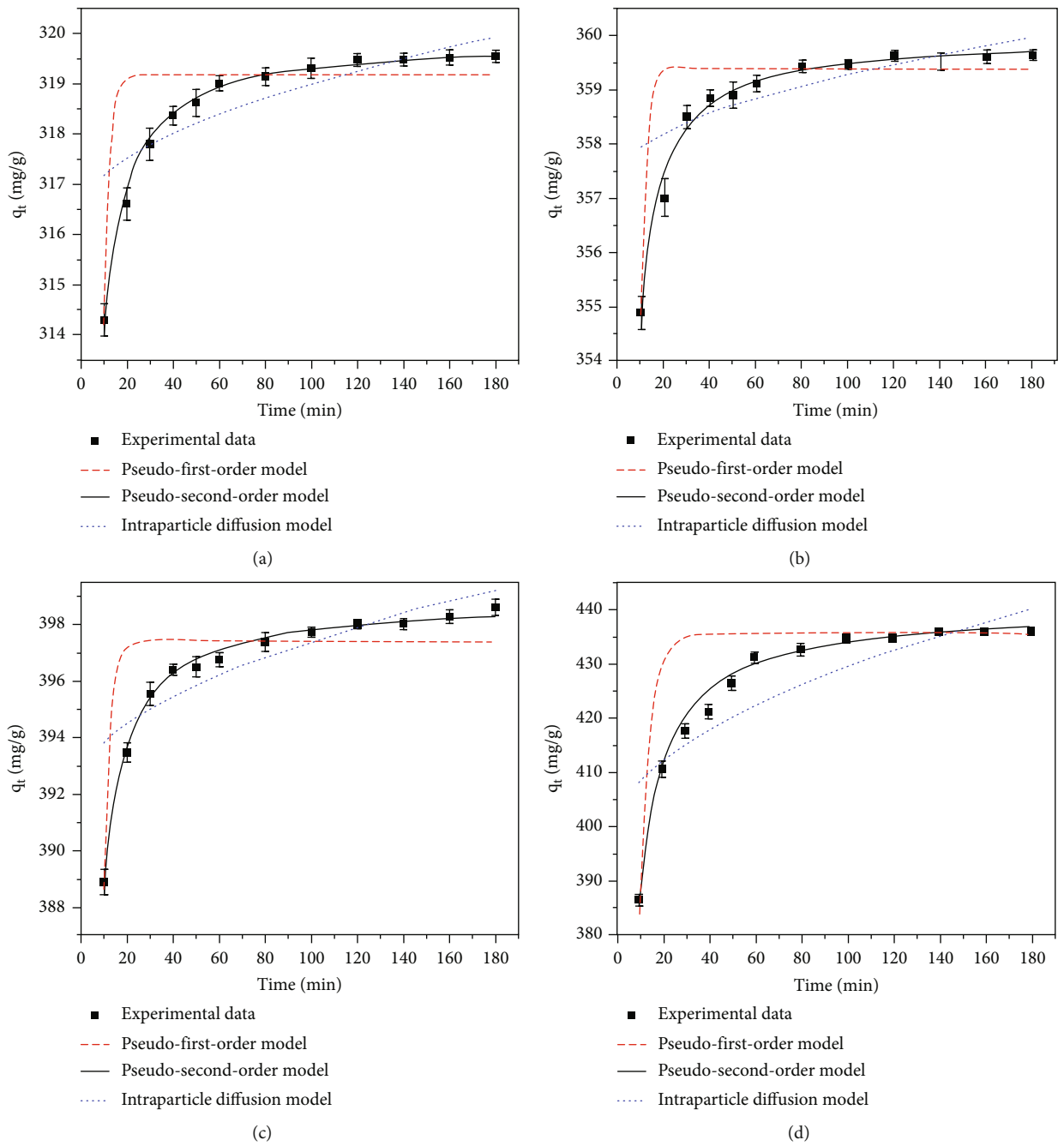

Figure 4: Fitted curves of kinetics models for different concentrations 800 mg/L (a), 900 mg/L (b), 1000 mg/L (c), and 1100 mg/L (d).

TEM image showed that $CaFe_2O_4$ consisted of irregular sheets of nanostructures and had a stacking phenomenon (Figure 1(b)), which was consistent with the SEM morphology. XRD pattern of $CaFe_2O_4$ nanosheets were shown in Figure 1(c). The presence of characteristic peaks located at $2\theta = 33.53^\circ$, 35.38°, 40.18°, 49.57°, 60.08°, and 61.22° matched well diffraction peaks of (320), (201), (131), (401), (600), and (161) planes of $CaFe_2O_4$ standard card (JCPDS. NO. 32-0168), which indicated that the $CaFe_2O_4$ was successfully prepared. The Ms value of $CaFe_2O_4$ (Figure 1(d)) was 8.15 emu/g, which was beneficial to the subsequent solid-liquid separation.

As could be seen from Figure 2(a), the $CaFe_2O_4$ was not formed at 400-500°C. When the calcination temperature reached 600°C, the $CaFe_2O_4$ begin to form gradually, but the crystallinity was very poor. With the calcination temperature was further risen to 700-800°C, the intensity of diffraction peaks was enhanced and the crystallinity was fine. Figure 2(b) showed the relationship between different calcination temperatures and saturation magnetizations. The saturation magnetization decreased with the calcination temperature increasing from 400 to 500°C. When the calcination temperature was between 600 and 700°C, $CaFe_2O_4$ started to form gradually and therefore the saturation magnetization

Table 1: Adsorption kinetics parameters of magnetic $CaFe_2O_4$ nanosheets with concentrations of MB solutions.

Kinetics model	Parameter	Initial MB concentration (mg/L)			
		800	900	1000	1100
Pseudo-first-order model	R^2	0.6987	0.7326	0.7438	0.7495
	k_1	0.4245	0.4442	0.3871	0.2220
	Adj. R-square	0.6686	0.7059	0.7182	0.7245
Pseudo-second-order model	R^2	0.9924	0.9878	0.9940	0.9898
	k_2	0.0171	0.0190	0.0097	0.0160
	Adj. R-square	0.9916	0.9866	0.9935	0.9888
Intraparticle diffusion model	R^2	0.7103	0.6476	0.7120	0.7369
	k_i	0.3957	0.3417	0.6932	3.8120
	C_i	0.5	0.5	0.5	0.5
	Adj. R-square	0.6813	0.6123	0.6833	0.7106

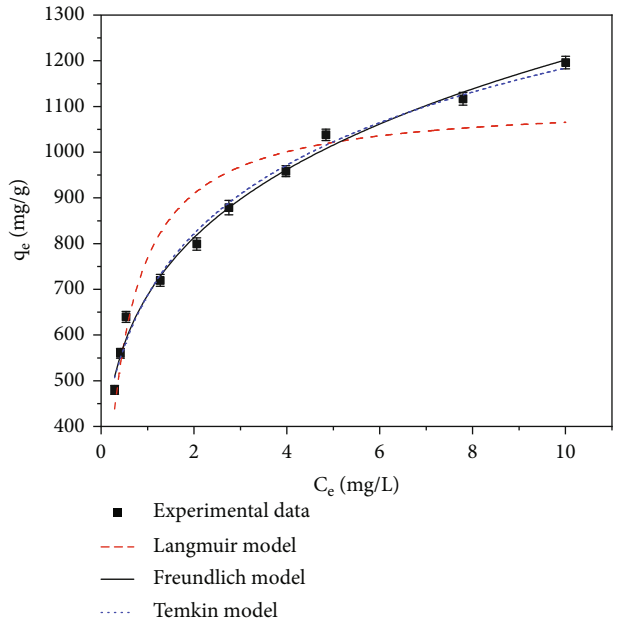

Figure 5: Langmuir, Freundlich, and Temkin isotherms for the adsorption of MB by $CaFe_2O_4$ nanosheets.

Table 2: Isotherm parameters of $CaFe_2O_4$ nanosheets for MB adsorption.

Isotherms model	R^2	Adj. R-square	Parameter	Parameter's value
Langmuir	0.8936	0.8803	q_{max}	1126.8135
			K_L	2.0191
Freundlich	0.9907	0.9895	$1/n$	0.2403
			K_F	689.1913
Temkin	0.9892	0.9862	A_T	41.0518
			b_T	191.9073

began to rise. The saturation magnetization of $CaFe_2O_4$ decreased and the coercivity increased at 800°C. This might be due to the excessive calcination temperature causing disorganization of the internal structure of the $CaFe_2O_4$ nanomaterials, which limited the growth of grain size. According to the Scherrer formula, the grain size of $CaFe_2O_4$ nanomaterials at 800°C was calculated to be 28.9 nm smaller than 700°C, which verified the above explanation. Therefore, the highest saturation magnetization was 8.15 emu/g at 700°C. In summary, $CaFe_2O_4$ with the calcination temperature of 700°C was selected for the subsequent experiments.

Table 3: Comparison of the maximum adsorption capacity of different adsorbents.

Adsorbent	Dye	q_{max} (mg/g)	References
Ni-MCM-41		189.04	[38]
$MnFe_2O_4$		497.51	[39]
$Co_{0.5}Zn_{0.5}Fe_2O_4$	Methyl blue	189.10	[40]
$Sr_{3x}Ba_{3x}(PO_4)_3/Fe_3O_4$		702.00	[41]
$CaFe_2O_4$		1126.81	In this article

3.2. Adsorption Kinetics. Figure 3 showed adsorption kinetics curves of $CaFe_2O_4$ nanosheets with different MB concentrations. It could be seen that with the beginning of adsorption, the adsorption capacity increased rapidly, and after a certain time, the adsorption capacity gradually slowed down until the adsorption achieved equilibrium. The reason was that at the beginning of the adsorption process, the material surface had many vacant adsorption and binding sites, and the greater the concentration of dye was, the stronger the mass transfer drive, resulted in a greater chance of contact between the MB molecules and the material. As the concentration of dye decreased, the driving force decreased and the adsorption sites were largely occupied, and the adsorption slowly reached equilibrium. The largest adsorption amount was 436.01 mg/g with the initial concentration of 1100 mg/L. The adsorption time was 60 min to reach adsorption equilibrium.

To further investigate the effect of adsorption time on adsorption capacity, the kinetics models were adopted to the data for fitting. The fitted curves for different kinetics models were shown in Figure 4. The correlation coefficients

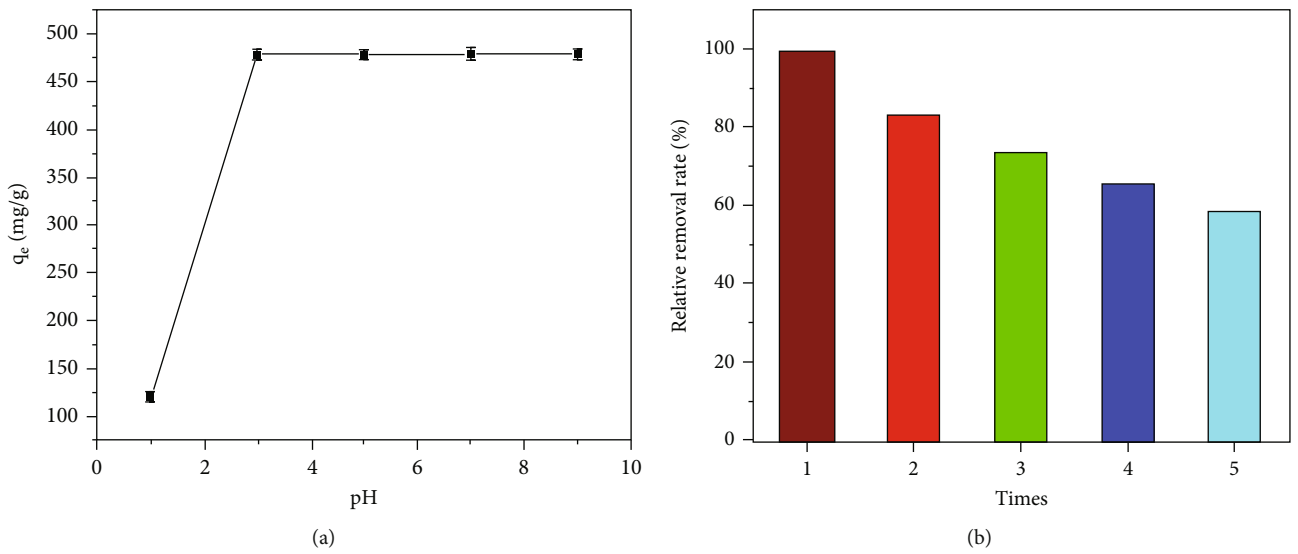

Figure 6: Effect of pH (a) and thermal regeneration (b) on the adsorption performance of $CaFe_2O_4$ nanosheets.

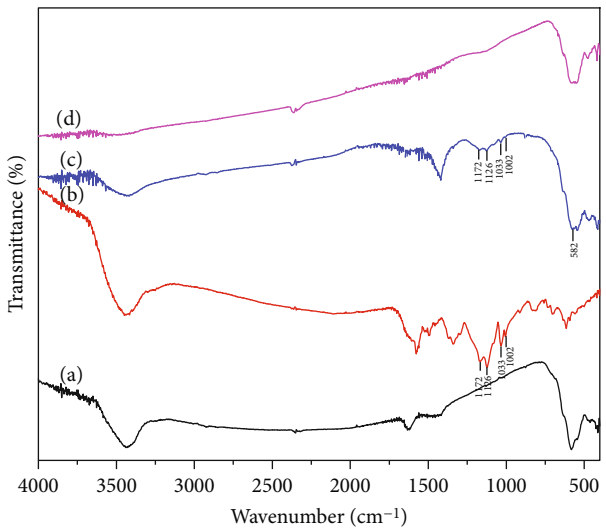

Figure 7: FTIR spectrum of $CaFe_2O_4$ nanosheets (a), MB (b), $CaFe_2O_4$ nanosheets after adsorption (c), and the regenerated $CaFe_2O_4$ nanosheets (d).

(R^2) of the pseudo-second-order kinetics model were the largest compared with the pseudo-first-order kinetics and intraparticle diffusion models, which indicated that the pseudo-second-order kinetics model could better describe the adsorption of on MB. According to the mechanism of the pseudo-second-order kinetics model, the adsorption of $CaFe_2O_4$ nanosheets on MB was chemisorption with electron gain and loss. The arguments fitted to three kinetics models were summarized as Table 1.

3.3. Adsorption Isotherms. The adsorption behaviors of the adsorbent for the dye can be evaluated with the adsorption isotherm model (Figure 5). The fitted parameters for the three models were displayed from Table 2. A comparison of the correlation coefficients (R^2) showed that the Freundlich model had the largest correlation coefficient of 0.9907. This suggested that the Freundlich model was consistent with isothermal adsorption processes. According to Freundlich theory, the adsorption between the dye molecules and the surface of the $CaFe_2O_4$ nanosheets was nonuniform. $1/n$ was in the range of 0.1-0.5, which indicated that the adsorption performance of $CaFe_2O_4$ nanosheets was excellent.

The maximum capacity was investigated by comparing the MB adsorption with other articles, it was observed that the $CaFe_2O_4$ nanosheets adsorption capacity of MB was much larger than those of the other adsorbents, which reflected that the superior adsorption performance of $CaFe_2O_4$ nanosheets, and the relevant data were listed in Table 3.

3.4. Adsorption Mechanism

3.4.1. Effect of pH and Thermal Regeneration Performance. The experiment kept the constants of $CaFe_2O_4$ nanosheets mass and MB concentration, and then the pH effect on the $CaFe_2O_4$ nanosheets adsorption of MB was explored, the results were shown in Figure 6(a). When the pH of the solution was below 3.0, the $CaFe_2O_4$ nanosheets exhibited an enhanced adsorption of MB as the pH value enhanced. The excellent capacity was observed at pH 3.0 with the adsorption capacity of $CaFe_2O_4$ nanosheets was 478.1 mg/g. This might be due to the fact that the $CaFe_2O_4$ nanosheets and dye molecules had positively charged at the same time when the pH was less than 3.0, which led to the strong electrostatic repulsion between $CaFe_2O_4$ nanosheets and dye molecules, thus the adsorption capacity of the $CaFe_2O_4$ nanosheets was decreased. With the increase of pH value, the positive charge held by the dye molecules progressively dropped, and the electrostatic repulsion also dropped, resulted in a gradual improvement in the capacity of adsorption of $CaFe_2O_4$ nanosheets. The adsorption of MB capacity by the adsorbent remained largely unchanged when pH was greater than 3, mainly attributable to the electrostatic attraction of the negatively charged dye and the positively charged $CaFe_2O_4$ and the saturation adsorption capacity of the $CaFe_2O_4$ nanosheets [36, 42].

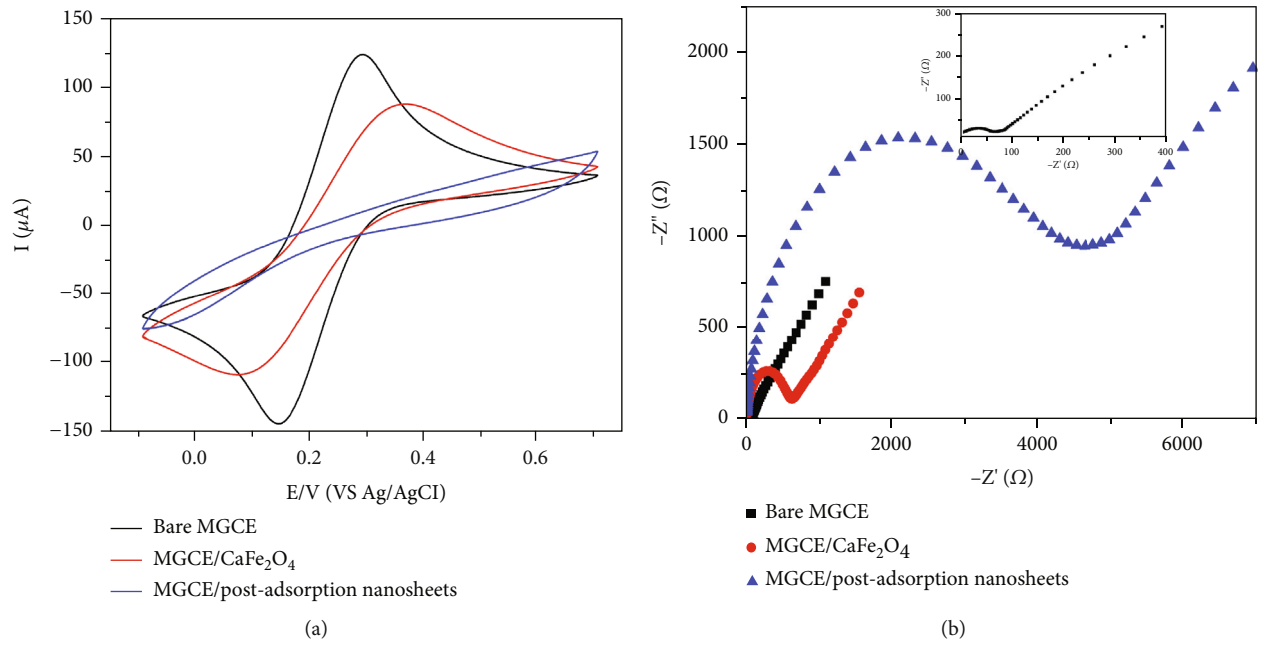

Figure 8: CV (a) and EIS (b) results of bare MGCE, MGCE/$CaFe_2O_4$, and MGCE/postadsorption nanosheets.

To research the regeneration performance of the $CaFe_2O_4$ nanosheets, the adsorbed $CaFe_2O_4$ nanosheets were regenerated by calcination treatment at 400°C for 2 h, and the readsorption results were shown in Figure 6(b). After five regenerations of $CaFe_2O_4$ nanosheets, the removal efficiency of MB was reduced to 59.06% of the first time. This was due to the increased crystallinity of the $CaFe_2O_4$ nanosheets and caused the collapse of the internal pores as the number of regenerations increased. These factors could cause the decrease of the specific surface area of $CaFe_2O_4$ nanosheets, resulted in a reduction in the surface area of contact from the MB molecules to the $CaFe_2O_4$ nanosheets and a consequent reduction in the adsorption capacity.

3.4.2. FTIR Analysis. FTIR spectrum of $CaFe_2O_4$ nanosheets, MB, $CaFe_2O_4$ nanosheets after adsorption, and regenerated $CaFe_2O_4$ nanosheets were shown in Figure 7. The peak appeared at 582 cm^{-1} corresponds to Fe-O bond and the bands at 3429 cm^{-1} was associated with −OH stretching vibration, indicated that the presence of residual water in $CaFe_2O_4$ nanosheets (Figure 7(a)). Figure 7(b) showed the FTIR spectrum of MB, the spectrum described some characteristic peaks at 1172 cm^{-1}, 1126 cm^{-1}, 1033 cm^{-1}, and 1002 cm^{-1}. The characteristic peaks of MB appeared on the FTIR spectrum of the adsorbed $CaFe_2O_4$ nanosheets indicated that MB was successfully adsorbed onto the $CaFe_2O_4$ nanosheets (Figure 7(c)). The regeneration results of the adsorbed $CaFe_2O_4$ nanosheets were presented in Figure 7(d). After calcination, the characteristic peak of MB disappeared completely, which indicated that the nanosheets could be regenerated by the mean of calcination.

3.4.3. Electrochemical Performance. The adsorption behavior of $CaFe_2O_4$ nanosheets on MB was further investigated by CV and EIS (Figure 8) [43–45]. The current formation was compared to that of the bare electrode by modifying $CaFe_2O_4$ on the surface of the glassy carbon electrode (MGCE/$CaFe_2O_4$) and the adsorbed $CaFe_2O_4$ nanosheets (MGCE/postadsorption nanosheets), the results were shown in Figure 8(a), where the bare MGCE had the highest peak current. The peak currents decreased sequentially with material and material modifications on the glassy carbon electrode. Ferrite nanomaterials were semiconductor materials with a high resistivity. When the materials were modified on the electrode surface, a certain spatial potential resistance was created, making it difficult for $[Fe(CN)_6]^{3-/4-}$ to approach the electrode surface, resulted in a decrease in peak current. After adsorption of MB, the nanomaterial was modified on the electrode surface and the negative charge carried by the MB and the $[Fe(CN)_6]^{3-/4-}$ were mutually repelled in the electrolyte, prevented it from approaching the surface of the electrode for electron switching and led to a peak current that was further reduced.

The electrochemical impedance spectrum consists of two parts, the semicircular part and the linear part. The electron transfer resistance can be obtained from the half-circle at high frequencies, and the linear at low frequencies corresponds to the diffusion process. As can be seen in Figure 8(b), the impedance of the bare electrode was lower compared to the impedance of the material and the material after adsorption of MB, and the impedance of the material after adsorption of MB was the highest. The results obtained were consistent with the CV plots.

4. Conclusions

$CaFe_2O_4$ nanosheets were prepared via a rapid combustion process. The $CaFe_2O_4$ nanosheets were formed under the conditions of calcination temperature of 700°C and ethanol volume of 50 mL, showed a lamellar morphology with an

average grain size of 93.3 nm, a thickness of 8.4 nm, and a saturation magnetization of 8.15 emu/g.

The adsorption of MB by $CaFe_2O_4$ nanosheets was eligible for the pseudo-second-order model and Freundlich model, which suggested that the adsorption process was multimolecular layer chemisorption and easy to adsorb. When the pH value was 3.0, the maximum adsorption capacity of $CaFe_2O_4$ nanosheets for MB was 478.07 mg/g. After five regenerations, the $CaFe_2O_4$ nanosheets still had a relative removal rate of 59.06%, which indicated excellent recyclability. This demonstrates that the prepared $CaFe_2O_4$ nanosheets were an adsorbent for dye wastewater with practical applications.

Data Availability

The research data used to support the finding of this study are included within the article.

Conflicts of Interest

The authors declare that they have no known competing financial interests or personal relationships that could have appeared to influence the work reported in this paper.

Authors' Contributions

Shaoshuai Zhang and Shuping Xu contributed equally to this work.

Acknowledgments

This work was supported by the Jiangsu Provincial Postgraduate Scientific Practice and Innovation Project (SJCX21_1722) and the Science and Technology Innovation Project of CHN Energy (GJNY-20-109).

Supplementary Materials

Supplementary data associated with this article can be found in the online version (*Supplementary Materials*). *(Supplementary Materials)*

References

[1] S. Yu, J. Y. Tang, Y. Wang, F. X. Xu, X. G. Li, and X. Z. Wang, "Recent advances in two-dimensional ferromagnetism: strain-, doping-, structural- and electric field-engineering toward spintronic applications," *Science and Technology of Advanced Materials*, vol. 23, no. 1, pp. 140–160, 2022.

[2] F. Xu, Y. Yang, Y. G. Liu et al., "Ferrite ceramic filled polydimethylsiloxane composite with enhanced magnetic- dielectric properties as substrate material for flexible electronics," *Ceramics International*, vol. 47, no. 13, pp. 18246–18251, 2021.

[3] D. E. Motaung, Z. P. Tshabalala, P. R. Makgwane et al., "Multifunctioning of CeO_2-SnO_2 heterostructure as room temperature ferromagnetism and chemiresistive sensors," *Journal of Alloys and Compounds*, vol. 906, article 164317, 2022.

[4] X. K. Wu, Z. Y. Wang, Y. Liu et al., "Enhanced performance of Bi_2Te_3-based thermoelectric materials by incorporating $Bi_2Fe_4O_9$ magnetic nanoparticles," *Journal of Alloys and Compounds*, vol. 904, article 163933, 2022.

[5] D. Kim, I. Efe, H. Torlakcik et al., "Magnetoelectric effect in hydrogen harvesting: magnetic field as a trigger of catalytic reactions," *Advanced Materials*, vol. 34, no. 19, article 2110612, 2022.

[6] D. L. Tian, T. Shi, X. Wang, H. Liu, and X. D. Wang, "Magnetic field-assisted acceleration of energy storage based on microencapsulation of phase change material with $CaCO_3/Fe_3O_4$ composite shell," *Journal of Energy Storage*, vol. 47, article 103574, 2022.

[7] Y. Padma, S. Nuthalapati, and U. S. Pantangi, "Synthesis and rheological characterization of nano-magnetorheological fluid using inverse spinel ferrite ($NiFe_2O_4$)," *International Journal of Applied Ceramic Technology*, vol. 19, no. 4, article 14031, pp. 1870–1878, 2022.

[8] U. Jamolov and G. Maizza, "Integral methodology for the multiphysics design of an automotive eddy current damper," *Energies*, vol. 15, no. 3, p. 1147, 2022.

[9] H. Morishita, T. Kohashi, H. Yamamoto, and M. Kuwahara, "Improvement of type-I method for observing magnetic contrast using scanning electron microscope under tilting-deceleration condition," *Journal of Magnetism and Magnetic Materials*, vol. 546, article 168733, 2022.

[10] Y. K. He, T. Helm, I. Soldatov et al., "Nanoscale magnetic bubbles inNd2Fe14Bat room temperature," *Physical Review B*, vol. 105, no. 6, article 064426, 2022.

[11] L. P. Liu, J. Cao, W. Guo, and C. Y. Wang, "Spin and spin–orbit coupling effects in nickel-based superalloys: a first-principles study on Ni_3Al doped with ta/W/re," *Chinese Physics B*, vol. 31, no. 1, article 016105, 2022.

[12] S. Thanikaikarasan, R. Kanimozhi, M. Saravannan, and R. Perumal, "Electrochemical deposition and characterization of CoNi alloy thin films," *Materials Today: Proceedings*, vol. 46, pp. 10248–10251, 2021.

[13] Y. Ahmad, B. Raina, S. Thakur, and K. K. Bamzai, "Magnesium and yttrium doped superparamagnetic manganese ferrite nanoparticles for magnetic and microwave applications," *Journal of Magnetism and Magnetic Materials*, vol. 552, article 169178, 2022.

[14] Y. X. Sun, J. B. Zhou, D. Liu, X. Li, and H. Liang, "Enhanced catalytic performance of Cu-doped $MnFe_2O_4$ magnetic ferrites: tetracycline hydrochloride attacked by superoxide radicals efficiently in a strong alkaline environment," *Chemosphere*, vol. 297, article 134154, 2022.

[15] A. K. Vishwakarma, B. Sen Yadav, J. Singh, S. Sharma, and N. Kumar, "Antibacterial activity of PANI coated $CoFe_2O_4$ nanocomposite for gram- positive and gram-negative bacterial strains," *Materials Today Communications*, vol. 31, article 103229, 2022.

[16] J. J. Xu, D. Liu, Y. B. Meng et al., "CoFe2O4nanoparticles dispersed on carbon rods derived from cotton for high-efficiency microwave absorption," *Nanotechnology*, vol. 33, no. 21, article 215603, 2022.

[17] A. Syed, A. H. Bahkali, and A. M. Elgorban, "Enhanced antibacterial and visible light driven photocatalytic activity of $CaFe_2O_4$ doped CdO heterojunction nanohybrid particles prepared by sono-chemical method," *Optical Materials*, vol. 113, article 110595, 2021.

[18] L. F. Guo, N. Okinaka, L. H. Zhang, and S. Watanabe, "Molten salt-assisted shape modification of $CaFe_2O_4$ nanorods for highly efficient photocatalytic degradation of methylene blue," *Optical Materials*, vol. 119, article 111295, 2021.

[19] Y. Sugawara, K. Kamata, A. Ishikawa, Y. Tateyama, and T. Yamaguchi, "Efficient oxygen evolution electrocatalysis on CaFe2O4and its reaction mechanism," *ACS Applied Energy Materials*, vol. 4, no. 4, pp. 3057–3066, 2021.

[20] A. L. Ma, L. Zhou, and E. J. Zhang, "Synthesis, magnetic and optical properties and photocatalytic activity of the polyacrylamide decorated CaFe2O4microspheres for photocatalytic degradation of organic wastewater," *Materials Research Express*, vol. 6, no. 7, article 075525, 2019.

[21] R. R. Wei, X. W. Lv, M. R. Yang, and J. Xu, "Effect of ultrasonic vibration treatment on solid-state reactions between Fe_2O_3 and CaO," *Ultrasonics Sonochemistry*, vol. 38, pp. 281–288, 2017.

[22] N. H. Sulaiman, M. J. Ghazali, J. Yunas, A. Rajabi, B. Y. Majlis, and M. Razali, "Synthesis and characterization of $CaFe_2O_4$ nanoparticles via co- precipitation and auto-combustion methods," *Ceramics International*, vol. 44, no. 1, pp. 46–50, 2018.

[23] L. L. Huang, Z. H. Fan, X. D. Li, S. Wang, and W. W. Guo, "Facile synthesis of $CaFe_2O_4$ nanocubes for formaldehyde sensor," *Materials Letters*, vol. 288, article 129351, 2021.

[24] W. J. Hua and Y. Kang, "Pulsed discharge plasma on water surface coupled with $CaFe_2O_4/Bi_2O_3$ composites for synergistic degradation of aqueous tetracycline hydrochloride," *Separation and Purification Technology*, vol. 279, article 119691, 2021.

[25] A. K. Das and A. Srinivasan, "Structural transition and associated magnetic properties of heat treated electrospun one-dimensional $CaFe_2O_4$," *Chemical Physics Letters*, vol. 786, article 139169, 2022.

[26] Y. Li, T. C. Wang, S. S. Zhang, Y. L. Zhang, L. L. Yu, and R. J. Liu, "Adsorption and electrochemical behavior investigation of methyl blue onto magnetic nickel-magnesium ferrites prepared via the rapid combustion process," *Journal of Alloys and Compounds*, vol. 885, article 160969, 2021.

[27] L. Y. Qiu, A. D. Phule, S. B. Wen, X. Zhang, Q. Chen, and Z. X. Zhang, "Multifunctional adsorbent: oleophobic latex sponge for removing dyes and Cu2+ from sewage waste," *Macromolecular Materials and Engineering*, vol. 306, no. 7, article 2100096, 2021.

[28] C. Zhao, H. T. Fu, X. H. Yang, S. X. Xiong, D. Z. Han, and X. Z. An, "Adsorption and photocatalytic performance of Au nanoparticles decorated porous Cu_2O nanospheres under simulated solar light irradiation," *Applied Surface Science*, vol. 545, article 149014, 2021.

[29] E. A. Afshar and M. A. Taher, "New fabrication of CuFe2O4/PAMAM nanocomposites by an efficient removal performance for organic dyes: kinetic study," *Environmental Research*, vol. 204, no. Part B, article 112048, 2022.

[30] L. Sun, S. C. Hu, H. M. Sun et al., "Malachite green adsorption onto Fe_3O_4@SiO_2-NH_2: isotherms, kinetic and process optimization," *RSC Advances*, vol. 5, no. 16, pp. 11837–11844, 2015.

[31] B. Kumar, K. Smita, S. Galeas et al., "Characterization and application of biosynthesized iron oxide nanoparticles using *Citrus paradisi* peel: A sustainable approach," *Inorganic Chemistry Communications*, vol. 119, article 108116, 2020.

[32] J. Poolwong, T. Kiatboonyarit, S. Achiwawanich, T. Butburee, P. Khemthong, and S. Kityakarn, "Three-dimensional hierarchical porous TiO_2 for enhanced adsorption and photocatalytic degradation of remazol dye," *Nanomaterials*, vol. 11, no. 7, p. 1715, 2021.

[33] Y. S. Yang, Y. Zhao, Y. Zong et al., "Activation of peroxymonosulfate by α-MnO_2 for Orange I removal in water," *Environmental Research*, vol. 210, article 112919, 2022.

[34] D. Talbot, J. Queiros Campos, B. L. Checa-Fernandez et al., "Adsorption of organic dyes on magnetic iron oxide nanoparticles. part I: mechanisms and adsorption-induced nanoparticle agglomeration," *ACS Omega*, vol. 6, no. 29, pp. 19086–19098, 2021.

[35] Q. Li, D. S. Yu, C. Y. Fan et al., "Gold nanoparticles adsorbed on graphene as nanozymes for the efficient elimination of dye pollutants," *ACS Applied Nano Materials*, vol. 5, no. 1, pp. 94–100, 2022.

[36] R. T. Kapoor, M. R. Salvadori, M. Rafatullah, M. R. Siddiqui, M. A. Khan, and S. A. Alshareef, "Exploration of microbial factories for synthesis of nanoparticles - a sustainable approach for bioremediation of environmental contaminants," *Frontiers in Microbiology*, vol. 12, article 658294, 2021.

[37] L. L. Yu, Y. Li, S. Pan, W. Huang, and R. J. Liu, "Adsorption mechanisms and electrochemical properties of methyl blue onto magnetic $Ni_xMg_yZn_{(1-x-y)}Fe_2O_4$ nanoparticles fabricated via the ethanol-assisted combustion process," *Water Air and Soil Pollution*, vol. 231, no. 6, p. 316, 2020.

[38] Y. H. Shu, Y. M. Shao, X. Y. Wei et al., "Synthesis and characterization of Ni-MCM-41 for methyl blue adsorption," *Microporous and Mesoporous Materials*, vol. 214, pp. 88–94, 2015.

[39] L. J. Yang, Y. Y. Zhang, X. Y. Liu et al., "The investigation of synergistic and competitive interaction between dye Congo red and methyl blue on magnetic $MnFe_2O_4$," *Chemical Engineering Journal*, vol. 246, pp. 88–96, 2014.

[40] P. Deng, M. Liu, and Z. X. Lv, "Adsorption mechanism of methyl blue onto magnetic $Co_{0.5}Zn_{0.5}Fe_2O_4$nanoparticles synthesized via the nitrate-alcohol solution combustion process," *AIP Advances*, vol. 10, no. 9, article 095005, 2020.

[41] F. Zhang, X. J. Yin, W. H. Zhang, and Y. F. Ji, "Optimizing decolorization of methyl blue solution by two magnetic hydroxyapatite nanorods," *Journal of the Taiwan Institute of Chemical Engineers*, vol. 65, pp. 269–275, 2016.

[42] A. Hamd, M. Shaban, H. AlMohamadi et al., "Novel wastewater treatment by using newly prepared green seaweed–zeolite nanocomposite," *ACS Omega*, vol. 7, no. 13, pp. 11044–11056, 2022.

[43] X. Liu, Y. Qiu, D. M. Jiang et al., "Covalently grafting first-generation PAMAM dendrimers onto MXenes with self-adsorbed AuNPs for use as a functional nanoplatform for highly sensitive electrochemical biosensing of cTnT," *Microsystems & Nanoengineering*, vol. 8, no. 1, p. 35, 2022.

[44] H. M. Fahmy, E. S. Abu Serea, R. E. Salah-Eldin et al., "Recent progress in graphene- and related carbon-nanomaterial-based electrochemical biosensors for early disease detection," *ACS Biomaterials Science & Engineering*, vol. 8, no. 3, pp. 964–1000, 2022.

[45] Y. L. Zhang, M. Liu, S. Pan, L. L. Yu, S. S. Zhang, and R. J. Liu, "A magnetically induced self-assembled and label-free electrochemical aptasensor based on magnetic Fe_3O_4/Fe_2O_3@Au nanoparticles for $VEGF_{165}$ protein detection," *Applied Surface Science*, vol. 580, article 152362, 2022.